Key Points:
- We study the small-scale magnetic fluctuations embedded within large-scale FACs
- We find the fluctuation intensity scales with large-scale FAC density
- The distribution of the fluctuations is controlled by magnetospheric activity

Correspondence to:
J. Wu,
jiashu.wu@ucalgary.ca

A comparison of small-scale magnetic fluctuations in the Region 1 and 2 field-aligned current systems

J. Wu[1] [ID], M. S. Bryant[1] [ID], C. G. Ridley[2] [ID], Y. Shen[1] [ID], L. Yang[3], L. B. N. Clausen[3] [ID], K. A. McWilliams[2] [ID], K. R. Murphy[4] [ID], I. R. Mann[5] [ID], L. G. Ozeke[5] [ID], H. Korth[6] [ID], B. J. Anderson[6] [ID], and C. L. Waters[7] [ID]

[1] Department of Physics and Astronomy, University of Calgary, Calgary, Alberta, Canada, [2] Institute of Space and Atmospheric Studies, University of Saskatchewan, Saskatoon, Saskatchewan, Canada, [3] Department of Physics, University of Oslo, Oslo, Norway, [4] NASA Goddard Space Flight Center, Greenbelt, Maryland, USA, [5] Department of Physics, University of Alberta, Edmonton, Alberta, Canada, [6] The Johns Hopkins University Applied Physics Laboratory, Laurel, Maryland, USA, [7] Department of Physical and Mathematical Sciences, University of Newcastle, Callaghan, New South Wales, Australia

Abstract By determining the location and size of the Region 1 (R1) and Region 2 (R2) large-scale field-aligned currents (FACs) from Active Magnetosphere and Planetary Electrodynamics Response Experiment data, we are able to study the small-scale magnetic fluctuations observed by the Swarm satellites embedded within the large-scale FACs. A statistical comparison of R1 and R2 high-frequency fluctuations is presented in terms of different solar wind conditions and geomagnetic activities. We find that (1) the amplitude of high-frequency fluctuations in both R1 and R2 increases as the large-scale R1 and R2 FACs intensify; (2) high-frequency fluctuations in R1 peak near dayside dawn and dusk, while those in R2 peak around noon; (3) the location of the largest high-frequency fluctuations in R1 shifts in local time in response to IMF B_y, indicating a connection between the R1 fluctuation and the driving solar wind most likely explained by magnetic reconnection; and (4) high-frequency fluctuations in R2 are enhanced in a small region near local noon and respond clearly to nightside drivers, as characterized by the auroral electrojet index. Our analysis shows that the intensity of R1 and R2 high-frequency magnetic fluctuations is directly connected to the intensity of FACs, which implies that the magnetic fluctuations are closely related to the magnetospheric processes that drive them.

1. Introduction

Magnetospheric field-aligned currents (FACs) have been determined using satellite magnetometer data since the 1970s. *Iijima and Potemra* [1976a] and *Iijima and Potemra* [1976b] studied FACs in the northern hemisphere using magnetometer data from the Triad satellite. They demonstrated that the transverse (east-west) magnetic perturbations were due to the satellite passing through electrical currents coupling the magnetosphere and ionosphere. They showed statistically that FACs were found to exist in two large concentric rings located at ~70° magnetic latitude. The poleward FACs were called Region 1 (R1) currents, and the equatorward FACs were called Region 2 (R2) currents. The polarity of the adjacent R1 and R2 FACs at the same local time was found to be opposite. The polarity of the FAC pair was also found to be reversed across the noon-midnight meridian. The large-scale downward R2 at lower latitudes and upward R1 FACs at higher latitudes occur on the dusk side, while upward R2 and downward R1 FACs occur on the dawn side. The location of these current systems corresponds approximately with the location of the auroral oval.

The large-scale dynamics of the R1 and R2 currents can be explained in the context of the large-scale ionospheric plasma circulation that is driven by magnetic reconnection with the interplanetary magnetic field (IMF) [*Dungey*, 1961]. The large-scale current system, including the FACs, is reviewed by *Cowley* [2000]. The R1 FACs occur near the large ionospheric convection reversal boundaries that map to near the magnetopause flanks, while the R2 FACs map within the magnetosphere to the ring current [*Iijima and Potemra*, 1978; *Cowley*, 2000].

While the large-scale R1 and R2 FACs connect the magnetosphere to the auroral ionosphere and respond to the large-scale dynamics of convection, the small-scale variations superimposed upon the large-scale currents

are important to understanding plasma dynamics [*Rother et al.*, 2007]. Small-scale FACs contribute to heating in the atmosphere and ionosphere, leading to neutral upwelling [*Lühr et al.*, 2004; *Kervalishvili and Lühr*, 2013] and ion upflow [*André et al.*, 1998]. The small-scale FACs are also related to auroral dynamics, such as fluctuating and pulsating aurora, which are the result of energetic particle scattering from the magnetosphere into the ionosphere [*Hasegawa*, 1976; *Sato et al.*, 2004]. They can also drive enhancements in the ionospheric conductivity through the ionospheric feedback instability [*Atkinson*, 1970; *Miura and Sato*, 1980]. *Nagatsuma et al.* [1996] suggested that the observed magnetic fluctuations in the poleward boundary region of the nightside auroral oval are a superposition of small-scale Alfvénic features and quasi-static currents. *Gjerloev et al.* [2011] performed a large global statistical analysis of the magnetic field fluctuations from the Space Technology 5 satellites. They examined the FAC correlations for different scale sizes and satellite separation times. They proposed that there is a different reconfiguration time of the magnetosphere on the dayside (60 s) and the nightside (160 s). They attribute this difference to different magnetospheric regimes and controls, with the dayside dominated by solar wind and reconnection processes and the nightside dominated by magnetotail plasma sheet processes.

The behavior of the large-scale R1 and R2 FAC systems under a variety of solar wind conditions and ranges of geomagnetic activity has been established [e.g., *Iijima and Potemra*, 1976a, 1978; *Anderson et al.*, 2008; *Clausen et al.*, 2012; *Coxon et al.*, 2014; *Carter et al.*, 2016]. Most studies have been statistical ensembles of single-satellite observations. Studies of FAC relying on magnetic field data from a single satellite must assume that the magnetic field variations are the result of the spacecraft traversing an infinitely long and stationary current sheet. Multiple satellites that orbit together, such as the Cluster and Swarm missions [*Dunlop et al.*, 2005; *Ritter and Lühr*, 2006; *Lühr et al.*, 2015; *Friis-Christensen et al.*, 2008], help to resolve small-scale spatial and temporal changes. *Lühr et al.* [2015] used Swarm data to divide FAC events into small-scale structures (with scale sizes smaller than 10 km), which are associated with kinetic Alfvén waves, and large-scale structures (larger than 150 km). The results of *Lühr et al.* [2015] were also consistent with the observation of *Ishii et al.* [1992] who reported a cutoff for kinetic Alfvén waves at periods between 4 and 10 s for a range of ionospheric conductivities. *Neubert and Christiansen* [2003] found that small-scale FACs (with spatial scales down to 600 m) are primarily located in the cusp region and are affected by IMF and solar wind turbulence. They also suggested that small-scale currents may be associated with significant local heating of the ionosphere and thermosphere. Using satellite data from CHAMP and DMSP, *Kervalishvili and Lühr* [2013] showed that the small-scale FACs depend on ionospheric conductivity in the cusp region and that they are related to Joule heating of the thermosphere resulting from dayside reconnection.

In a recent study by *Carter et al.* [2016] the location of the large-scale R2 FACs from Active Magnetosphere and Planetary Electrodynamics Response Experiment (AMPERE) data were found to be more consistent with the location of auroral UV emissions than the R1 FACs. *Rother et al.* [2007] used magnetic field data from CHAMP satellite and focused on kilometer-scale FACs in the range from 5 km to below 1 km. They found that these kilometer-scale FACs are predominantly accompanied by downward FACs in the morning sector and by upward FACs in the afternoon sector. These authors demonstrated that the majority of kilometer-scale FACs reside in large-scale R1 current system. These studies show that there is a requirement to distinguish between the large-scale R1 and R2 FACs when investigating small-scale FAC dynamics.

Following proof-of-concept studies [*Anderson et al.*, 2000; *Waters et al.*, 2001], the AMPERE mission [*Anderson et al.*, 2014] used magnetic field data from the Iridium constellation of 66 satellites to produce global maps of large-scale FACs. In the present study, the AMPERE FAC data will be used to identify the large-scale R1 and R2 FAC regions globally. Within these larger-scale FAC regions, the higher-resolution magnetic field data from the Swarm mission will be used to study the small-scale magnetic fluctuations.

2. Data Sets

The Iridium commercial satellite constellation consists of 66 satellites in equally spaced circular polar orbits at an altitude of 780 km. *Anderson et al.* [2000] and *Waters et al.* [2001] used Iridium data to derive the large-scale FACs poleward of 40° magnetic latitude in both hemispheres. These studies provided the proof-of-concept that resulted in the AMPERE scientific mission in which the Iridium data are used to produce a high-quality global FAC data set [*Anderson et al.*, 2008]. The AMPERE data set produces FAC maps with values along each magnetic local time (MLT) with a resolution of 1° of magnetic latitude (MLAT). These maps are suitable for identifying large-scale R1 and R2 FACs globally.

The ability to resolve smaller magnetic fluctuations within the large-scale FAC regions is provided by the Swarm mission, a constellation composed of three identical satellites (A, B, and C). Swarm was launched by European Space Agency in late November 2013 [*Olsen et al.*, 2013]. Swarm A and Swarm C fly in tandem at a lower altitude of 460 km. They are separated by approximately 1.4° longitude and a 10 s in time along track. Swarm B flies solo at a higher altitude of 510 km. Each satellite is equipped with a magnetometer and provides 1 Hz and 50 Hz magnetic field data and Level-2 FAC data. The single-satellite FAC data are calculated according to Ampere's law using the east-west component of the magnetic field data after removal of a mean magnetic field. The assumptions to derive FACs include (1) that the currents are static and spatial features; (2) the current sheet has an infinite plane geometry along the east-west direction; and (3) the FACs flow in sheet perpendicular to the satellite's orbit plane. Since the events in this study cover the R1 and R2 FAC regions in the entire northern hemisphere, the assumption of infinite and static current sheets may not be valid for all the events. Besides, the angle between the orientation of the FAC sheet and the satellite trajectory varies from orbit to orbit, which introduces additional uncertainty to the FAC data for to each orbit, making it hard to quantify the uncertainty of the FAC data in a statistical study. To reduce the uncertainty introduced by the processing of the Level-2 FAC data product, the 1 Hz magnetic field data from individual Swarm satellites was used in this study. The spectrum of 50 Hz FAC presented by *Rother et al.* [2007] showed that there is virtually no wave power above 8 Hz and that it is nearly constant at lower frequencies, indicating that the 1 Hz magnetic data are sufficient to resolve the kilometer-scale FACs we aim to investigate.

3. Methodology

In this paper, the smaller-scale magnetic field fluctuations measured by Swarm are examined in the context of the large-scale R1 and R2 FACs from AMPERE. In one orbit Swarm will pass through the auroral zone four times, twice in the north and twice in the south. Because of its high inclination, the passes are nearly meridional. This study includes northern passes only. For each pass through the auroral zone, the average time and MLT of the Swarm pass is used to determine the most appropriate meridional FAC profile from AMPERE for comparison. The locations of the large-scale FACs are determined from the R1/R2 bipolar FAC fitting technique of *Clausen et al.* [2012]. The AMPERE FAC maps have a 2 min cadence. However, each map requires 10 min of magnetic field data to produce global FAC maps. During active period the FACs can change dramatically in 10 min [e.g., *Murphy et al.*, 2012]. To ensure the stability of the FACs within these 10 min windows, the R1/R2 bipolar fitting technique is applied to three FAC profiles at the nearest MLT of the Swarm pass: (1) the nearest 2 min FAC map during the Swarm pass, (2) a 10 min average from five FAC maps centered on the nearest 2 min FAC map during the Swarm pass, and (3) the sum of five FAC maps centered on the nearest 2 min FAC map during the Swarm pass. For the purpose of this study we consider the AMPERE fits to be stable if two of three methods produce similar bipolar fits, such that the large-scale FACs are quasi-stationary over a 10 min window.

As per the method of *Clausen et al.* [2012], the widths (w) of the FAC profiles, i.e., the widths of the R1 and R2 current sheets, and zero crossings (ZC) were calculated. The FAC profile was considered stable if $|ZC_1 - ZC_2| < 0.5°$ or $|ZC_1 - ZC_3| < 0.5°$ and if $|w_1 - w_2| < 0.5°$ or $|w_1 - w_3| < 0.5°$, where the indices refer to the three FAC profiles. This selection method yielded 10,732 good passes in the northern hemisphere and 3727 in the southern hemisphere. Due to the eccentricity of the Iridium orbits the AMPERE fits tend to be less reliable in the southern hemisphere than in the northern hemisphere *Anderson et al.* [2008]. This can create errors in the identification of the bipolar R1 and R2 current system. Thus, for this study we restrict the analysis of Swarm magnetic field perturbations and identification of R1/R2 bipolar fits to the northern hemisphere only, because the northern AMPERE FAC maps are more reliable.

An example of the FAC identification in relation to a Swarm pass is presented in Figure 1. In Figure 1 (top), magnetic field data from Swarm A (green) and Swarm C (purple) during one pass through the dawnside R1/R2 current region are presented. The dashed grey line is the nearest 2 min meridional FAC profile from AMPERE. The solid grey line is the R1/R2 bipolar fit to the AMPERE FAC profile. The R1 and R2 FAC sheets determined from the bipolar fit are highlighted with light red and blue shading, respectively. The MLAT boundary between R1 and R2 is the average of the three zero crossings calculated for this pass (ZC_1, ZC_2, and ZC_3). As explained later, we chose the width w of the R1/R2 current sheets to be 4°.

We calculated the power spectra inside the R1 and R2 FAC regions for all passes using a fast Fourier transform (FFT) of the east-west magnetic field data in north-east-center frame of the satellite. Example spectra are presented in Figures 1d and 1e. For each pass, the mean magnetic field component within the window was
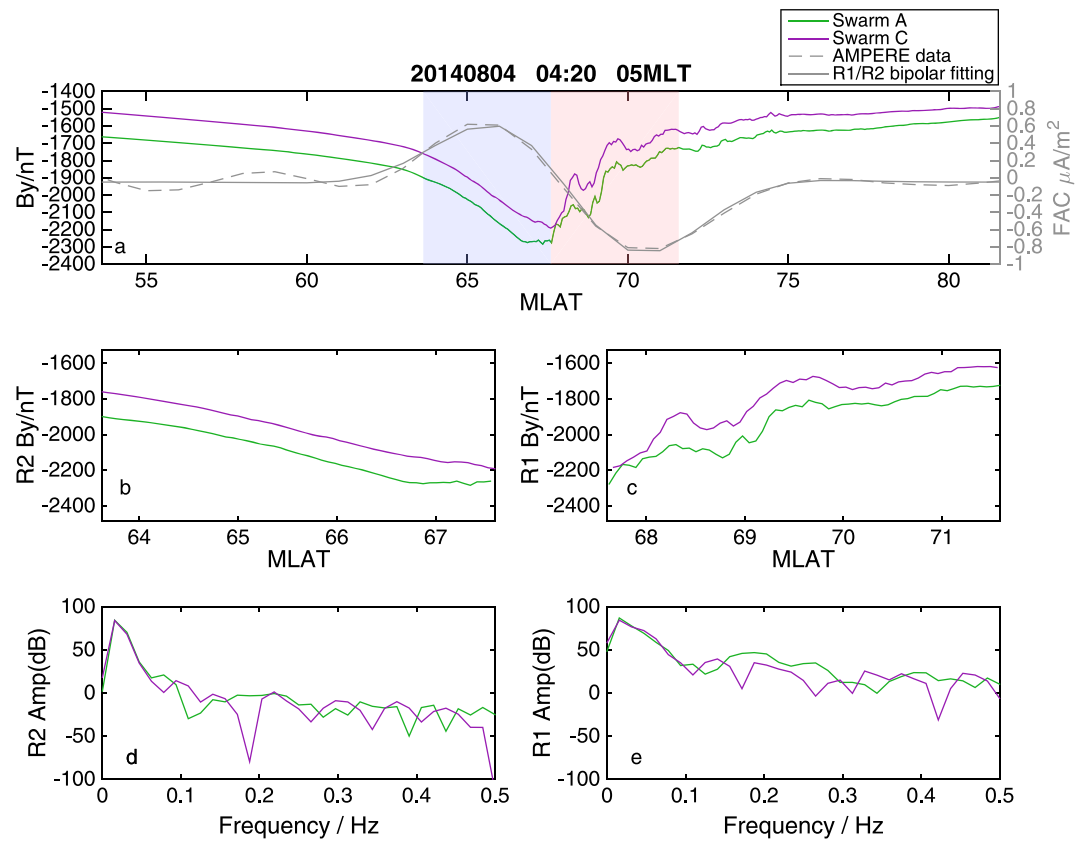
Figure 1. The green and purple lines in Figure 1a show magnetic field data for a paired set of Swarm A and Swarm C passes as a function of geomagnetic latitude (MLAT). The dashed and solid grey lines are the large-scale AMPERE data time series and the R1/R2 bipolar fits. The red- and blue-shaded areas correspond to the 4° window used for R1 and R2, respectively. Figures 1b and 1c show enlargements of the blue (R2) and red (R1) shaded regions, respectively. Figures 1d and 1e show the power spectra for R2 and R1, respectively. The spectrum is separated into high- and low-frequency parts according to the cutoff frequency of 0.0163 Hz. The high-frequency amplitude ($\overline{A_{hf}}$) and low-frequency amplitude ($\overline{A_{lf}}$) are obtained by average the amplitude of high- and low-frequency spectra. Note that R1 has a higher spectral amplitude than R2 for both high- ($\overline{A_{hf}}$) and low-frequency ($\overline{A_{lf}}$) spectra.

subtracted, and a Hanning window was applied prior to calculating the FFT. The 4° MLAT (or 62 s) window determines the 0.0163 Hz cutoff between what we define in this study to be the low- and high-frequency portions of the spectra. The high- and low-frequency portions of the spectra are each averaged to obtain an estimate of the spectral amplitude in both frequency ranges, which are referred to as the high-frequency amplitude ($\overline{A_{hf}}$) and low-frequency amplitude ($\overline{A_{lf}}$) throughout the manuscript. The common window size for R1 and R2 allows their spectral amplitudes to be easily compared. Note that in Figure 1 the R1 FAC has a larger high-frequency amplitude than R2, which is representative of the passes included in the study. In the subsequent sections, the high- and low-frequency amplitudes are used to study variations statistically in the R1 and R2 high- and low-frequency spectra under varying driving conditions.

To justify our choice of a constant 4° width (w) of the R1 and R2 current sheets, the distribution of the FAC widths determined from the bipolar profile fitting method as a function of MLT is presented in Figure 2. On the dayside, the FAC regions tend to be narrower, and the FACs are typically at higher latitudes. The median of the width distribution as a function of MLT is represented by the solid line and the upper and lower quartiles by the dashed lines. The majority of FAC widths are larger than 4° MLAT, which is equivalent to 62 s or 488 km along the satellite track. Based on this width distribution, a common 4° width in MLAT was used to define the lower limit of the width of the large-scale R1 and R2 FAC sheets and hence the FFT window for all spacecraft passes used in this study. This common width across both FAC regions for all passes simplified the comparison of the power spectra. This common width is (1) narrow enough to remove the lower frequency data associated with the large-scale R1/R2 structure, (2) small enough to ensure that we analyzed data in a region that falls
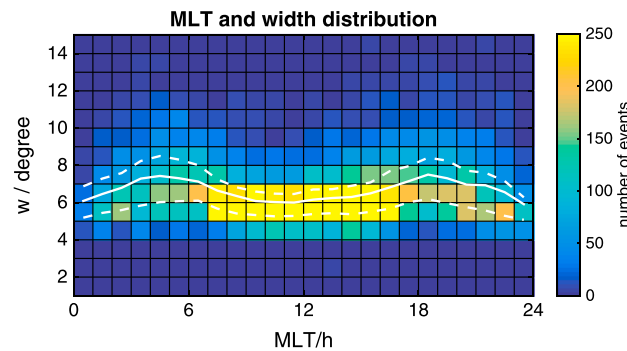
Figure 2. Distribution by MLT of the w values for all good northern hemisphere Swarm passes. The white line shows the median width at each MLT, and the dashed lines show the quartiles. The width varies with MLT with the majority of large-scale FACs being wider than 4° MLAT.

properly within the R1 or R2 location (i.e., not polar cap or subauroral data), and (3) large enough to give a good representation of the high-frequency fluctuations in the region.

4. Results

4.1. Characteristics of High-Frequency Magnetic Field Fluctuations From Swarm

In this paper, we present single-satellite magnetometer data from all three Swarm satellites for all good passes through the R1/R2 current regions in the northern hemisphere as defined in section 3. The measurements were made between December of 2013 and December of 2015, inclusive.

Figure 3 is the distribution of the bipolar-fitted peak current density of the nearest 2 min FAC profile from AMPERE for R1 and R2 FACs as a function of MLT for all Swarm passes used in this study. Negative FAC densities correspond to currents flowing vertically down into the northern ionosphere, and positive ones to FACs flowing vertically up out of the ionosphere. The color scale represents the occurrence rate of the FAC densities, and the white line indicates the median FAC density at each MLT. The R1 FAC (Figure 3a) flows into the ionosphere near dawn and out of the ionosphere near dusk, while the R2 FAC (Figure 3b)
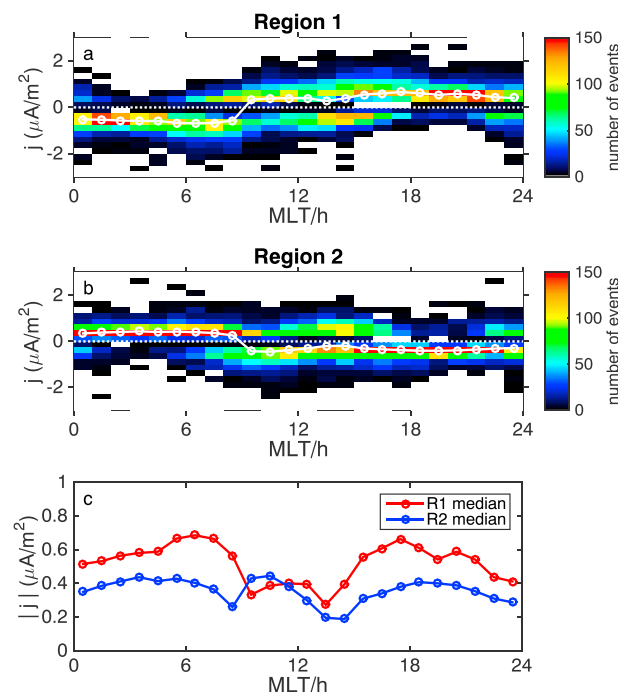

Figure 3. Histograms of peak fitted FAC density j ($\mu A/m^2$) from AMPERE in the northern hemisphere as a function of MLT for (a) R1 and (b) R2. Negative FAC densities correspond to flow into the ionosphere, and vice versa. The white line with open circles represents the median FAC density. The white dashed line is where j is 0 $\mu A/m^2$. The color bar shows the occurrence of events, binned per hour MLT and per 0.25 $\mu A/m^2$. (c) A comparison between Region 1 (red) and Region 2 (blue) of the absolute median FAC density as a function of MLT.

flows out of the ionosphere near dawn and into the ionosphere near dusk. Figure 3c is a comparison of the absolute values of the median of current densities. R1 FACs (red) tend to be larger than R2 (blue) at all local times, except in the noon sector where the FACs are comparable. These results are consistent with the FAC distributions presented by *Iijima and Potemra* [1978] and with the dominance of R1 over R2 current density as shown by *Coxon et al.* [2014]. They demonstrate that the automatic detection of R1 and R2 FACs with the bipolar FAC profile fitting technique produces a set of events that is consistent with the expected global FAC pattern.

The occurrence histograms of high-frequency amplitude ($\overline{A_{hf}}$) of the Swarm magnetic field data for all good passes in the northern hemisphere are presented in Figure 4. The occurrence distribution of the high-frequency spectral amplitude is a function of the peak current density from the bipolar fits with the AMPERE FAC profiles. The straight line represents the linear fit of the distribution, and the lines with circles represent the median of the histogram for each FAC magnitude bin. For both R1 and R2, the trend for increasing high-frequency amplitude ($\overline{A_{hf}}$) with increasing FAC density
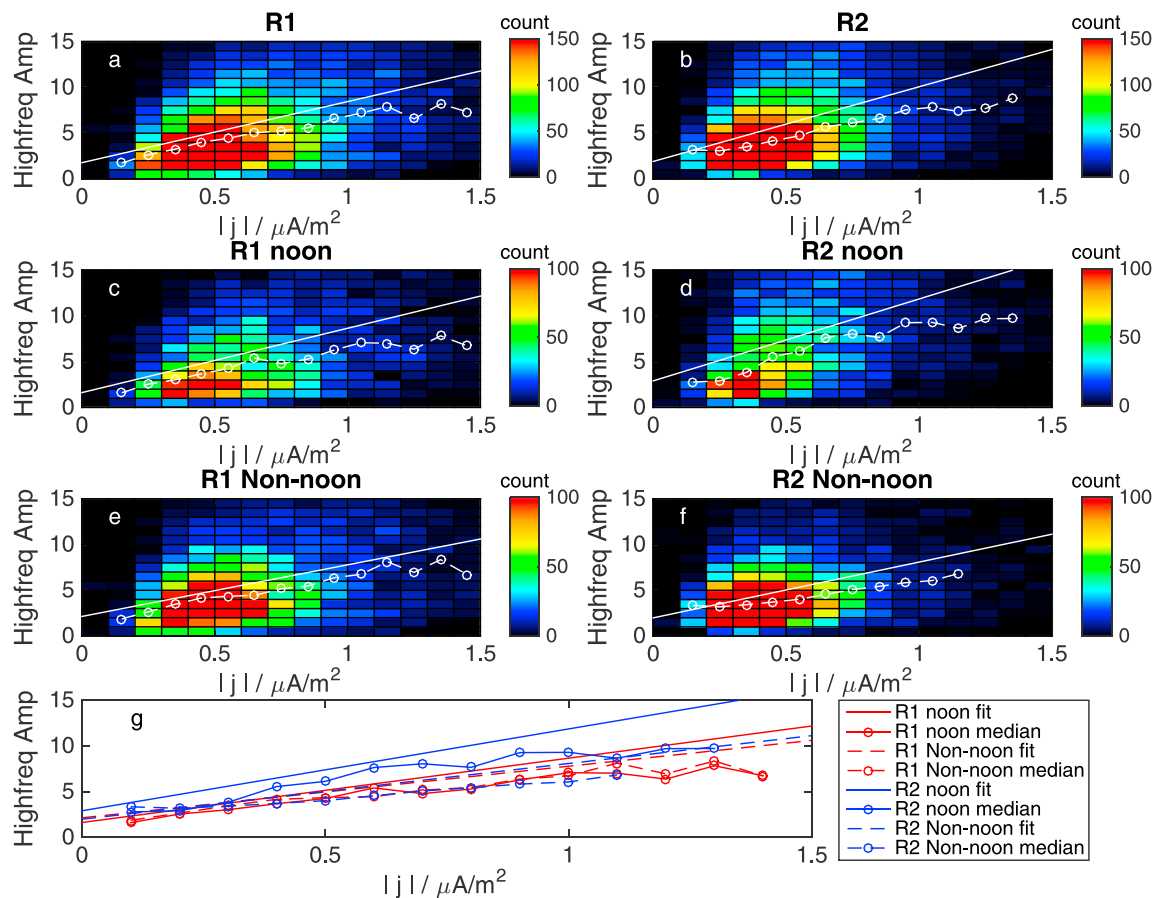
Figure 4. The occurrence distribution of high-frequency amplitude ($\overline{A_{hf}}$) in arbitrary units for (a) R1 and (b) R2 FACs as a function of FAC density in μA/m². The straight white line represents the linear regression of the distribution. The lines with circles represent the median of the histogram. (c and d) The distributions of R1 and R2 high-frequency amplitude in the noon sector (8–16 MLT). (e and f) The distributions in the non-noon sector (0–7 MLT and 17–24 MLT). (g) A comparison of linear fits and median values of the R1 and R2 high-frequency amplitude for the noon sector and non-noon sector.

demonstrates that high-frequency magnetic field fluctuations are larger when the magnitude of the large-scale FAC is larger. Because of the different behavior near noon, which is evident in Figure 3, the histograms were subdivided into a region in the noon sector (8–16 MLT, Figures 4c and 4d) and a region away from noon ("non-noon": 0–7 MLT and 17–24 MLT, Figures 4e and 4f). Both R1 and R2 distributions have similar slopes away from noon, but the R2 fluctuations in the noon sector (Figures 4d and 4g) have a higher slope than all other distributions.

4.2. Influence of Solar Wind and Geomagnetic Conditions on High-Frequency Fluctuations

Using the spectral amplitudes of the Swarm magnetic field spectra, we investigate the influence of solar wind conditions and geomagnetic activity on the large-scale (low-frequency spectral amplitude $\overline{A_{lf}}$) and small-scale (high-frequency spectral amplitude $\overline{A_{hf}}$) magnetic field variations in R1 and R2.

To investigate the interplanetary magnetic field (IMF) influence on R1 and R2 FACs, we classified the events according to the IMF clock angle, defined by $\theta = \arctan(B_y/B_z)$ (Figures 5 and 6). Clock angles between [−45, 45] and [135, −135]° correspond to IMF quadrants of dominant IMF +B_z and −B_z, respectively (Figure 6). Clock angles between [+45, +135] and [−135, −45]° correspond to IMF quadrants of dominant IMF +B_y and −B_y, respectively (Figure 5). In Figures 5a and 5c and 6a and 6c, we present the low-frequency (large-scale) amplitudes in R1 and R2. In Figures 5b and 5d and 6b and 6d in both figures we present the high-frequency (small-scale) amplitudes in R1 and R2.

There is very little difference between the low-frequency amplitude for the two IMF B_y orientations in R1 and R2. The low-frequency amplitude tends to be marginally higher near noon for both FAC types and all B_y conditions. The R1 high-frequency amplitude (Figure 5b) depends on the orientation of IMF B_y. The high-frequency
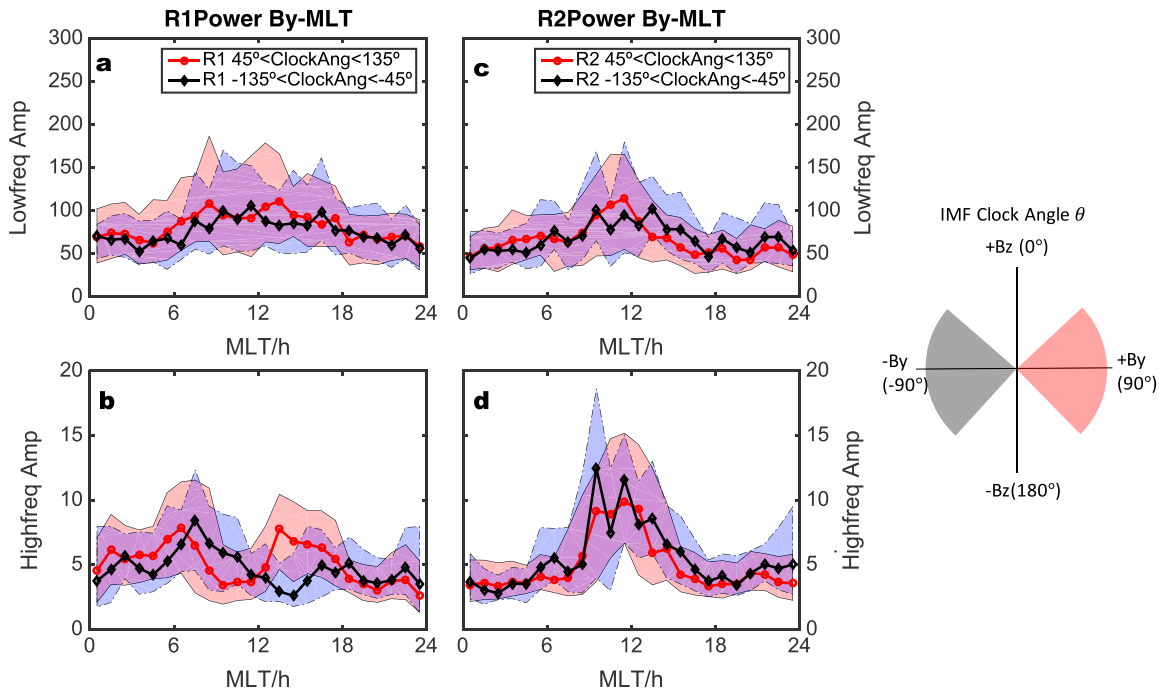
Figure 5. High-frequency amplitude ($\overline{A_{hf}}$) and low-frequency amplitude ($\overline{A_{lf}}$) for R1 and R2 FACs as a function of MLT and IMF clock angle ($\theta = \arctan(B_y/B_z)$). The solid lines represent the median values, and the upper and lower quartiles are indicated by the shaded regions. (a) Low-frequency spectral amplitude ($\overline{A_{lf}}$) in R1 for positive (red) and negative (black) IMF B_y. (b) High-frequency spectral amplitude ($\overline{A_{hf}}$) in R1 for positive (red) and negative (black) IMF B_y. (c) Low-frequency spectral amplitude ($\overline{A_{lf}}$) in R2 for positive (red) and negative (black) IMF B_y. (d) High-frequency spectral amplitude ($\overline{A_{hf}}$) in R2 for positive (red) and negative (black) IMF B_y.

Figure 6. (a) Low-frequency spectral amplitude ($\overline{A_{lf}}$) in R1 for northward (black) and southward (red) IMF. (b) High-frequency spectral amplitude ($\o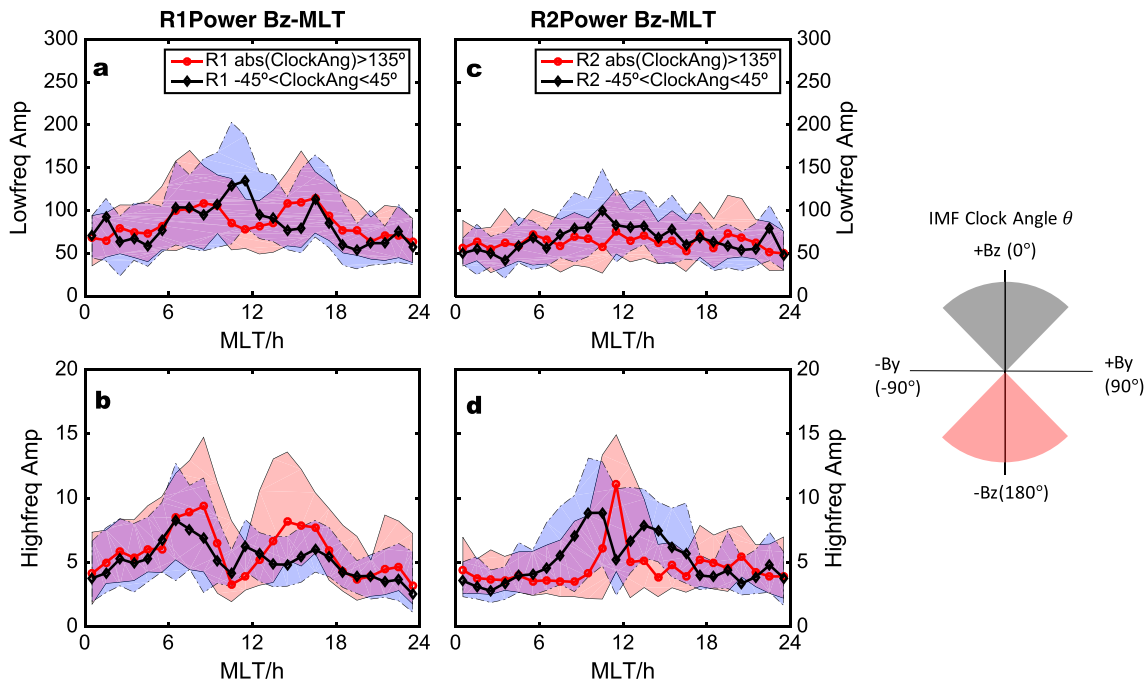verline{A_{hf}}$) in R1 for northward (black) and southward (red) IMF. (c) Low-frequency spectral amplitude ($\overline{A_{lf}}$) in R2 for northward (black) and southward (red) IMF. (d) High-frequency spectral amplitude ($\overline{A_{hf}}$) in R2 for northward (black) and southward (red) IMF.
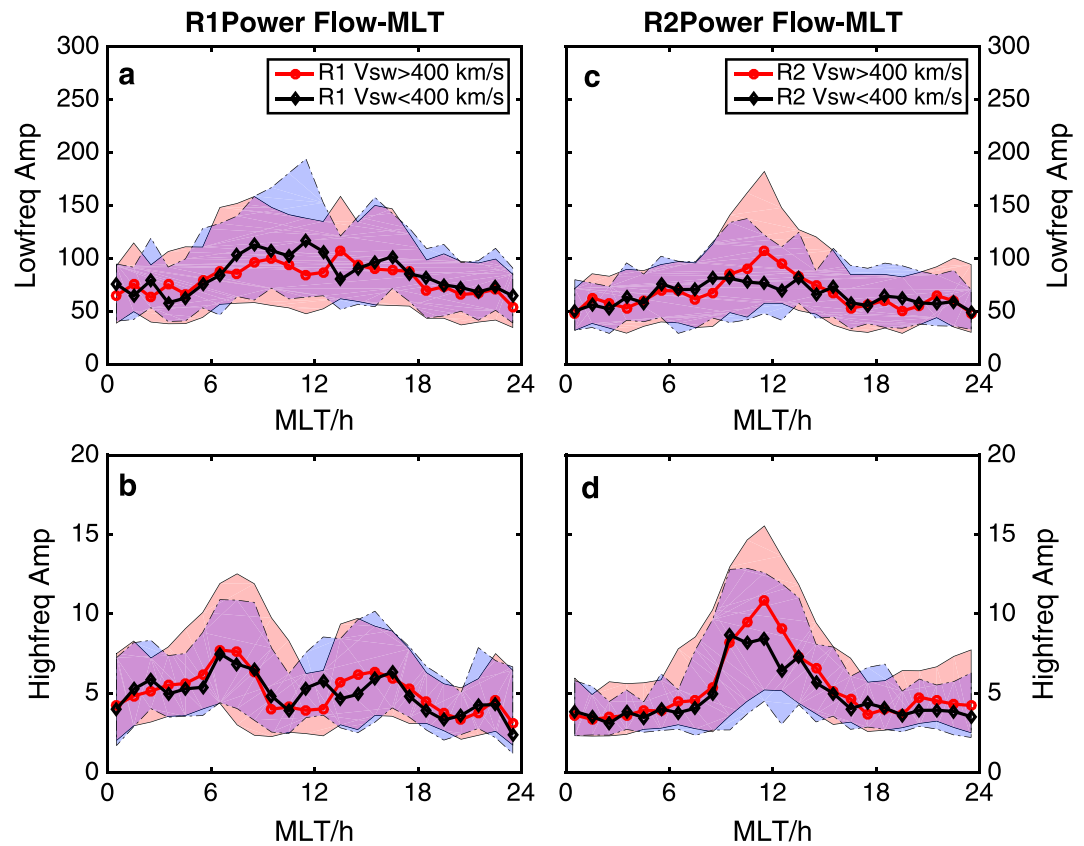
Figure 7. Spectral amplitude separated by high- and low-frequency, R1 and R2, and solar wind velocity in km/s. The threshold between fast flow (red) and slow flow (black) is taken at 400 km/s. The solid lines represent the median, while the upper and lower borders of the shaded regions represent the upper and lower quartiles, respectively. Statistics for (a) low-frequency amplitude ($\overline{A_{lf}}$) in R1, (b) high-frequency amplitude ($\overline{A_{hf}}$) in R1, (c) low-frequency amplitude ($\overline{A_{lf}}$) in R2, and (d) high-frequency amplitude ($\overline{A_{hf}}$) in R2.

spectral amplitude of the R1 FACs reverses across local noon, with the IMF $+B_y$ spectral amplitude dominating in the postnoon region and the IMF $-B_y$ spectral amplitude dominating in the prenoon region (Figure 5b). The high-frequency amplitude of R2 FACs is similar for both orientations of IMF B_y, and both amplitudes are large near local noon (Figure 5d).

For the IMF B_z positive and negative quadrants in Figure 6, there are differences between the low-frequency R1 and R2 FACs in the noon sector. The low-frequency R2 FACs are not dependent on IMF B_z (Figure 6c), but the R1 low-frequency amplitude enhances near noon for the IMF $+B_z$ (black line in Figure 6a) and peaks at the dayside flanks at MLT 10 and 14 for IMF $-B_z$ (red line in Figure 6a). High-frequency amplitude in R1 displays two peaks on the dayside flanks which are enhanced and closer to noon during IMF $-B_z$ (red line in Figure 6b). High-frequency amplitude in R2 displays a prominent narrow peak at noon for the $-B_z$ zone and a broader enhancement around noon for the $+B_z$ zone but dips at the exact location of the $+B_z$ peak (Figure 6d).

Through Figure 7, we investigate the effects of solar wind flow speed as a driver for high- and low-frequency fluctuations in R1 and R2 FACs, using a threshold separation at flow speeds above (red) and below (black) 400 km/s. Figures 7a and 7c show only minimal differences between high and low flow speeds in low-frequency amplitudes for both R1 and R2. Figures 7b and 7d show flank and noon enhancements for all solar wind speeds, respectively. Flow speed therefore seems to produce no noticeable differences in large- and small-scale FAC variations in the time scales we consider.

In Figure 8, we use a threshold separation of solar wind dynamic pressures above (red) and below (black) 2 nPa to investigate the dynamic pressure as a possible driver for amplitude variations in R1 and R2. Figures 8a and 8c show minimal differences between high and low dynamic pressures for low-frequency amplitudes in R1 and R2 on average. However, Figures 8b and 8d display enhancements for high-frequency amplitude in
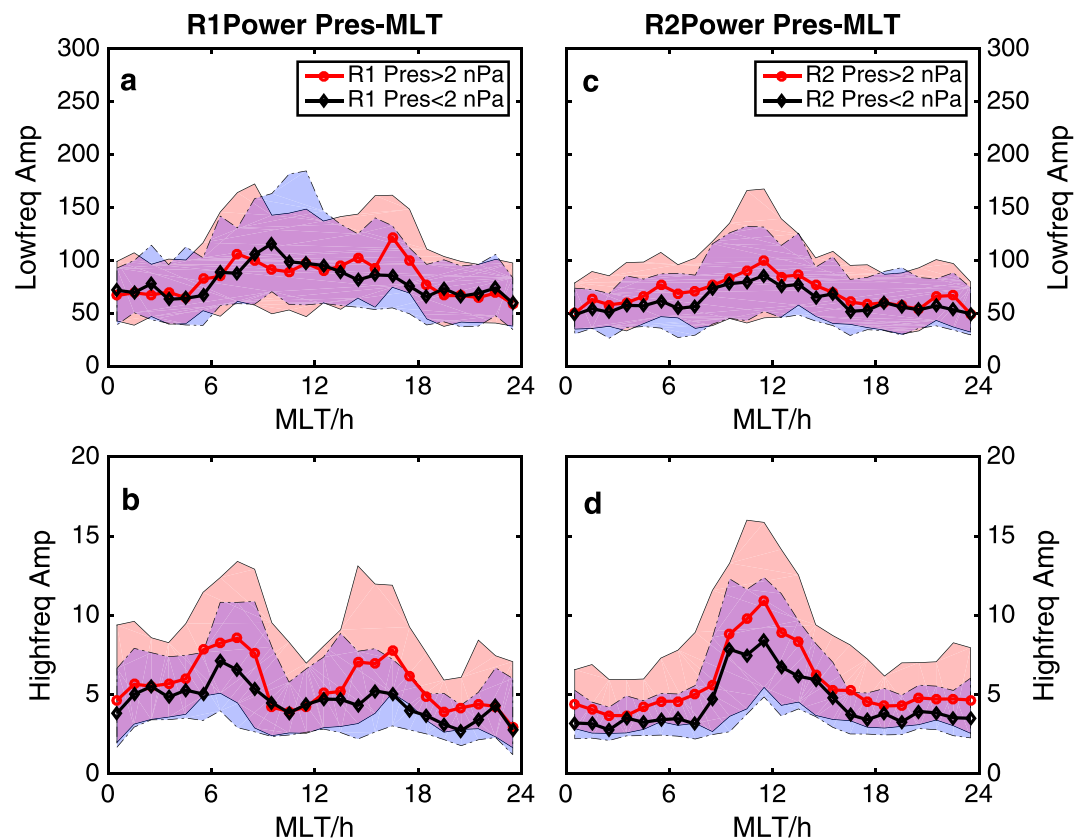
Figure 8. Spectral amplitude separated by high- and low-frequency, R1 and R2, and solar wind dynamic pressure in nanopascals. The threshold between high pressure (red) and low pressure (black) is taken at 2 nPa. The solid lines represent the median, while the upper and lower borders of the shaded regions represent the upper and lower quartiles, respectively. Statistics for (a) low-frequency amplitude $(\overline{A_{\mathrm{lf}}})$ in R1, (b) high-frequency amplitude $(\overline{A_{\mathrm{hf}}})$ in R1, (c) low-frequency amplitude $(\overline{A_{\mathrm{lf}}})$ in R2, and (d) high-frequency amplitude $(\overline{A_{\mathrm{hf}}})$ in R2.

both R1 and R2 at nearly all MLT when dynamic pressures are larger than 2 nPa (see the upper quartiles in Figure 8b and 8d). This pattern is not shown for data sorted by high solar wind velocities in Figure 7.

Finally, in Figure 9 we present the AE index to investigate the effects of enhanced convection on magnetic fluctuations in FACs. We take AE index above 300 nT (red) as indicative of enhanced global convection and below 300 nT (black) as indicative of baseline convection levels. We find in Figure 9a that the low-frequency amplitudes in R1 peak near noon for low AE but peak at the flanks for high AE. In Figure 9b, we find that the R1 high-frequency amplitude also peak at the flanks for high AE, but we do not find the low AE peak at noon, as in Figure 9a. The difference is minimal between high and low AE for low frequencies in R2, as seen in Figure 9c. In Figure 9d, we see a narrower and stronger peak at noon and also nightside enhancements for high AE in R2 high-frequency amplitude.

5. Discussion

In this study we use 1 s cadence magnetic field data from Swarm to quantify the large- and small-scale magnetic field fluctuations in the R1 and R2 FACs. "Large-scale" fluctuations have scale size of the order of the R1 and R2 FACs themselves, while "small-scale" refers to all the fluctuations smaller than that. We use the AMPERE global FAC database to distinguish the locations of the R1 and R2 current systems for each Swarm pass through that region. This approach makes it possible to investigate the low-frequency (0–0.0163 Hz) and high-frequency (0.0163–0.5 Hz) magnetic field variations in each FAC region independently. The separation frequency of 0.0163 Hz is determined by the 4° width of the current sheet and the cutoff frequency of 0.5 Hz is the Nyquist frequency. By investigating the behavior of both low- and high-frequency R1 and R2 FAC amplitudes under different magnetospheric conditions, we find that, in general, stronger solar wind driving and
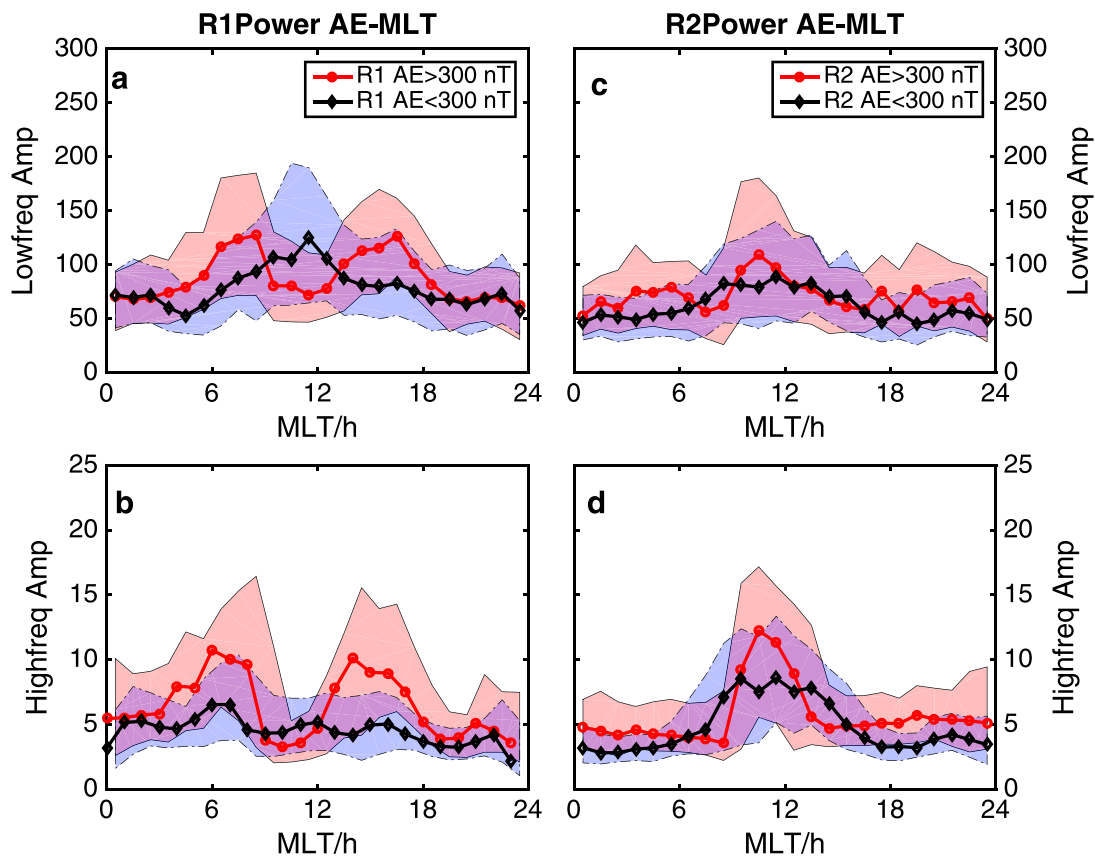
Figure 9. Magnetometer power amplitude separated by high- and low-frequency, R1 and R2, and enhanced nightside convection index *AE* in nanoteslas. The threshold between high activity (red) and low activity (black) is taken at 300 nT. The solid lines represent the median, while the upper and lower borders of the shaded regions represent the upper and lower quartiles, respectively. Show statistics for (a) low-frequency amplitude ($\overline{A_{\mathrm{lf}}}$) in R1, (b) high-frequency amplitude ($\overline{A_{\mathrm{hf}}}$) in R1, (c) low-frequency amplitude ($\overline{A_{\mathrm{lf}}}$) in R2, and (d) high-frequency amplitude ($\overline{A_{\mathrm{hf}}}$) in R2.

increased geomagnetic activity lead to an enhancement of the high-frequency magnetic field fluctuations in the R1/R2 FACs.

The FAC magnitudes in Figure 3c show that the R1 FAC maximizes near dawn and dusk. The R2 FAC also peaks near dawn and dusk, and it has an additional enhancement near local noon. The first large-scale statistical FAC distributions obtained from Triad satellite passes [*Iijima and Potemra*, 1978] revealed the enhancements near dawn and dusk. *Anderson et al.* [2014] confirmed this on a global scale using the multispacecraft AMPERE magnetic field data.

The amplitude of the high-frequency fluctuations ($\overline{A_{\mathrm{hf}}}$) in R1 and R2 increase as the peak FAC intensity increases, as shown in Figure 4. This demonstrates that stronger FACs tend to contain more high-frequency magnetic field fluctuations in both R1 and R2. The high-frequency fluctuations could be carrying a substantial portion of the FACs [*Neubert and Christiansen*, 2003] in both R1 and R2.

The maximum intensity of the R1 FAC peaks near dawn and dusk (Figure 3c). We therefore expect enhanced R1 high-frequency power near dawn and dusk, because the high-frequency amplitude scales with the intensity of the FACs (Figure 4). These enhancements are evident in Figures 5b, 6b, 7b, 8b, and 9b.

Unlike R1, the R2 FAC has a local FAC enhancement at noon, as well as at dawn and dusk (Figure 3c). We would therefore expect the R2 high-frequency amplitude to peak near noon, as well as near dawn and dusk. However, there is a peak in the R2 high-frequency amplitude near noon but not near dawn and dusk (see Figures 5d, 6d, 7d, 8d, and 9d). Both R1 and R2 have similar scaling factors between FAC peak density and high-frequency amplitudes at all local times, but the R2 fluctuations in the noon sector (Figures 4d and 4g) have a higher scaling factor such that for the same FAC amplitude the high-frequency power is larger in the R2 current than it is in the R1 current. This may explain the noon enhancement of R2 high-frequency fluctuations.

Previous studies have also reported significant small-scale FAC densities near magnetic local noon [e.g., *Neubert and Christiansen*, 2003; *Kervalishvili and Lühr*, 2013]. *Neubert and Christiansen* [2003] reported that small-scale FACs are very intense in the cusp, regularly $10-100\,\mu A/m^2$ and reaching $1\,mA/m^2$ during disturbed conditions. This is 1 or 2 orders of magnitude greater than the large-scale FACs. The small-scale FACs may therefore play a large role in the heating of the ionosphere and thermosphere. *Kervalishvili and Lühr* [2013] investigated the influence of small-scale currents on the cusp neutral density anomaly. They observed the largest-amplitude small-scale (1 Hz) FAC densities near noon. *Rother et al.* [2007] reported that the occurrence of kilometer-scale FAC maximizes at the peak of large-scale FACs and that kilometer-scale FACs occur preferably in connection with R1 FACs in the dawn and dusk sectors. Their results are consistent with the relationship between large- and small-scale FACs we demonstrated in Figure 4 and the dominant R1 FACs at dawn and dusk in Figures 5–9. Our results further demonstrate that the magnitude of R1 away from noon mapping to the flanks are controlled by IMF, solar wind pressure, and *AE* index. However, no preference for FAC direction was shown at noon in *Rother et al.* [2007]. Further studies will be required to investigate if there is a physical process behind the enhanced fluctuations in R2 near noon or if they are due to a misidentification of the R1 and R2 FACs near noon using the automated FAC detection technique. Near noon the FAC sheets are highly structured, containing both R1 and R2 FACs as well as Region 0 (R0) FACs [*Iijima and Potemra*, 1976b]. This complicated structuring of FAC sheets cannot be routinely characterized by the bipolar fitting used in this study, which assumes the presence of only two FACs. A detailed investigation of the noon sector is required to disentangle the R0/R1/R2 current system in this region. However, as this current study is a comparison of the nominal bipolar R1/R2 current systems, we leave this work to future studies.

The R1 high-frequency fluctuations are strongly affected by the orientation of the IMF B_y component (Figure 5). For positive B_y (red line in Figure 5b), the R1 high-frequency amplitude is largely symmetric with a slight preference of larger amplitudes in the postnoon sector. However, for negative B_y there is a clear asymmetry across noon where the high-frequency amplitude peaks in the prenoon sector (black line in Figure 5b). The R1 high-frequency amplitudes show much smaller peaks at the prenoon sector during low dynamic pressure (black line in Figure 8b) and low *AE* condition (black line in Figure 9b) and display symmetric enhancement on the flanks when the pressure and *AE* are high (red line in Figures 8b and 9b). The MLT location of these enhancements are consistent with the expected shift away from noon of the ionospheric footprint of the dayside reconnection site when IMF B_y is large [e.g., *Heppner and Maynard*, 1987; *Newell et al.*, 1989; *Cowley and Lockwood*, 1992]. When there is a dominant IMF $-B_y$ component, the reconnection footprint in the northern hemisphere shifts toward dawn. In comparison, the R2 high-frequency field fluctuations do not appear to be influenced by IMF B_y. In general, R1 FACs map to the magnetopause, while R2 FACs map to the ring current where the solar wind influence is expected to be much smaller. This implies a close connection between magnetopause reconnection processes and the small-scale R1 field fluctuations that we observe on either side of noon.

The R1 and R2 field fluctuations also respond to IMF B_z (Figure 6b) and geomagnetic activity as quantified by *AE* (Figure 9b). Both parameters are related to the strength of the global convection pattern. The R1 fluctuations peak near 9 and 15 MLT for southward IMF, while the R1 fluctuations have broader peaks that are shifted further away from noon for large *AE*. The *AE* index represents the occurrence of substorms in the nightside magnetosphere [*Kamide and Akasofu*, 1983] as well as the strength of the convection globally, driven by both dayside and nightside reconnection [e.g., *McWilliams et al.*, 2008; *Kissinger et al.*, 2011]. On the other hand, the R1 fluctuations during $-B_z$ conditions are enhanced closer to magnetic local noon, which is strongly related to the IMF B_z-driven reconnection on the dayside [*Milan et al.*, 2007]. In a statistical study *Coxon et al.* [2014] investigated the influence of magnetic reconnection on the large-scale FACs from AMPERE. They found that the FACs intensify as the *AL* index decreases (and the *AE* index increases) and as the dayside reconnection rate increases. The enhanced fluctuations that we observed are consistent with the enhanced FACs reported by *Coxon et al.* [2014].

For R2, the high-frequency fluctuations are enhanced around noon for all *AE* and B_z conditions (Figures 9d and 6d). The R2 peaks are narrower for $-B_z$ and larger *AE*. There is also a consistent enhancement of the R2 high- and low-frequency fluctuations at all MLTs away from noon when *AE* is high (Figures 9c and 9d). This is not evident in the B_z comparison (Figures 6c and 6d). These results suggest that the enhancements in the R2 high-frequency amplitudes are the result of substorms and enhanced nightside convection.

The comparison of solar wind speed and dynamic pressure effects on magnetic field fluctuations (see Figures 7 and 8) highlights that the high-frequency fluctuations in R1 and R2 respond strongly to increased solar wind dynamic pressure but not to increased solar wind speed. Higher solar wind dynamic pressure promotes small-scale R1 and R2 fluctuations at nearly all MLT. *Neubert and Christiansen* [2003] found that the solar wind turbulence (the root-mean-square value of the product $V_{SW}B_z$) contributes to the intensification of small-scale FAC. However, this solar wind turbulence parameter cannot rule out the influence of large $-B_z$ to R1 and R2 fluctuations, as discussed above. Figure 7 suggests that the solar wind speed plays very little role in the generation of magnetic field fluctuations in R1 and R2. High dynamic pressure, on the other hand, compresses the magnetosphere, enhances convection and currents, and excites wave activity [e.g., *Sibeck*, 1990; *Kivelson and Southwood*, 1991]. It is therefore not unexpected that the R1 and R2 fluctuations are enhanced during high dynamic pressure intervals.

In addition to the results presented in this paper, we also analyzed the seasonal distribution of the high-frequency magnetic field fluctuations from SWARM. R2 FACs have 1.3 times larger high-frequency amplitude in summer than in winter. This is consistent with previous studies [e.g., *Kervalishvili and Lühr*, 2013]. The difference is due to increased photoionization-related conductivity in the summer ionosphere. However, we do not see a similar seasonal dependence in the R1 fluctuations. This could result from our data processing methods, which do not directly compare events in adjacent Swarm passes in winter and summer hemispheres. This type of study would need to compare events on a case-by-case basis, which is beyond the scope of the present analysis.

Based on the data presented above, we demonstrated that the small-scale magnetic field fluctuations in both R1 and R2 are primarily controlled by the strength of global convection, which is driven by magnetic reconnection on both the dayside and nightside. Stronger convection leads to stronger large-scale FACs, which we have shown are associated with enhanced high-frequency magnetic field fluctuations. We have also shown that high solar wind dynamic pressure enhances R1 and R2 high-frequency magnetic field fluctuations at all MLTs.

6. Conclusion

By determining reliably the location and size of the R1 and R2 FACs from AMPERE for a large number of events, we were able to differentiate the magnetic field fluctuations observed by Swarm satellites embedded in R1 and R2 and determine how they respond to various solar wind and magnetospheric drivers. The technique that we have developed can be applied to other data sets, including low-altitude satellite and ground-based observations.

The statistical results show the following:

1. The large-scale R1 and R2 FAC magnitudes maximize near dawn and dusk, with R1 FAC larger than R2 at all MLT except in the noon sector.
2. The amplitude of the high-frequency fluctuations in R1 and R2 scales with the maximum intensity of the large-scale FAC sheets. The scaling factor in the R2 noon sector is larger than in all other regions. These high-frequency fluctuations play an important role in carrying large-scale FACs and are likely closely related to the processes driving the FAC especially during active times.
3. The enhanced high-frequency fluctuations in R1 are shifted prenoon or postnoon according to the orientation of the IMF B_y, which is consistent with the expected shift of the dayside magnetopause reconnection site.
4. High solar wind dynamic pressure increases the high-frequency fluctuations in R1 and R2, but the solar wind speed has little effect. High dynamic pressure compresses the magnetosphere, enhancing convection and currents and exciting wave activity.
5. The enhancement of R1 high-frequency fluctuations during both southward IMF B_z and high geomagnetic activity conditions (large *AE*) occurs along the flanks. This is evidence of increased convection globally, in response to enhanced reconnection on both the dayside and the nightside. R2 high-frequency fluctuations only show enhancement on the nightside when *AE* is high, indicating R2 is mainly controlled by the nightside driver.

Small-scale FACs contribute to various atmospheric and ionospheric processes and are related closely to large-scale FACs. The fundamental reason for difference responses in R1 and R2 high-frequency fluctuations

relates to the different regions in the magnetosphere where they flow. The R1 FAC maps to the magnetopause where the plasma motion is dominated by the $E \times B$ convection drift. The R2 FAC maps to the ring current where the particle motion is dominated by the curvature-gradient drift. The responses of the magnetopause and ring current to different drivers determine the behavior of R1 and R2 FAC and their embedded high-frequency fluctuations.

References

Anderson, B. J., K. Takahashi, and B. A. Toth (2000), Sensing global Birkeland currents with Iridium© engineering magnetometer data, *Geophys. Res. Lett.*, *27*, 4045–4048, doi:10.1029/2000GL000094.

Anderson, B. J., H. Korth, C. L. Waters, D. L. Green, and P. Stauning (2008), Statistical Birkeland current distributions from magnetic field observations by the Iridium constellation, *Ann. Geophys.*, *26*(3), 671–687, doi:10.5194/angeo-26-671-2008.

Anderson, B. J., H. Korth, C. L. Waters, D. L. Green, V. G. Merkin, R. J. Barnes, and L. P. Dyrud (2014), Development of large-scale Birkeland currents determined from the active magnetosphere and planetary electrodynamics response experiment, *Geophys. Res. Lett.*, *41*, 3017–3025, doi:10.1002/2014GL059941.

André, M., P. Norqvist, L. Andersson, L. Eliasson, A. I. Eriksson, L. Blomberg, R. E. Erlandson, and J. Waldemark (1998), Ion energization mechanisms at 1700 km in the auroral region, *J. Geophys. Res.*, *103*(A3), 4199–4222, doi:10.1029/97JA00855.

Atkinson, G. (1970), Auroral arcs: Result of the interaction of a dynamic magnetosphere with the ionosphere, *J. Geophys. Res.*, *75*(25), 4746–4755, doi:10.1029/JA075i025p04746.

Carter, J. A., S. E. Milan, J. C. Coxon, M.-T. Walach, and B. J. Anderson (2016), Average field-aligned current configuration parameterized by solar wind conditions, *J. Geophys. Res. Space Physics*, *121*, 1294–1307, doi:10.1002/2015JA021567.

Clausen, L. B. N., J. B. H. Baker, J. M. Ruohoniemi, S. E. Milan, and B. J. Anderson (2012), Dynamics of the region 1 Birkeland current oval derived from the Active Magnetosphere and Planetary Electrodynamics Response Experiment (AMPERE), *J. Geophys. Res.*, *117*, A06233, doi:10.1029/2012JA017666.

Cowley, S. W. H. (2000), Magnetosphere-ionosphere interactions: A tutorial review, in *Magnetospheric Current Systems*, vol. 118, edited by S.-I. Ohtani et al., pp. 91–106, AGU, Washington, D. C.

Cowley, S. W. H., and M. Lockwood (1992), Excitation and decay of solar wind-driven flows in the magnetosphere-ionosphere system, *Ann. Geophys.*, *10*(1–2), 103–115.

Coxon, J. C., S. E. Milan, L. B. N. Clausen, B. J. Anderson, and H. Korth (2014), The magnitudes of the regions 1 and 2 Birkeland currents observed by AMPERE and their role in solar wind-magnetosphere-ionosphere coupling, *J. Geophys. Res. Space Physics*, *119*, 9804–9815, doi:10.1002/2014JA020138.

Dungey, J. W. (1961), Interplanetary magnetic field and the auroral zones, *Phys. Rev. Lett.*, *6*, 47–48, doi:10.1103/PhysRevLett.6.47.

Dunlop, M. W., et al. (2005), Cluster observations of the CUSP: Magnetic structure and dynamics, *Surv. Geophys.*, *26*, 5–55, doi:10.1007/s10712-005-1871-7.

Friis-Christensen, E., H. Lühr, D. Knudsen, and R. Haagmans (2008), Swarm—An earth observation mission investigating geospace, *Adv. Space Res.*, *41*(1), 210–216, doi:10.1016/j.asr.2006.10.008.

Gjerloev, J. W., S. Ohtani, T. Iijima, B. Anderson, J. Slavin, and G. Le (2011), Characteristics of the terrestrial field-aligned current system, *Ann. Geophys.*, *29*(10), 1713–1729, doi:10.5194/angeo-29-1713-2011.

Hasegawa, A. (1976), Particle acceleration by MHD surface wave and formation of aurora, *J. Geophys. Res.*, *81*(28), 5083–5090, doi:10.1029/JA081i028p05083.

Heppner, J. P., and N. C. Maynard (1987), Empirical high-latitude electric field models, *J. Geophys. Res.*, *92*(A5), 4467–4489, doi:10.1029/JA092iA05p04467.

Iijima, T., and T. A. Potemra (1976a), The amplitude distribution of field-aligned currents at northern high latitudes observed by Triad, *J. Geophys. Res.*, *81*(13), 2165–2174, doi:10.1029/JA081i013p02165.

Iijima, T., and T. A. Potemra (1976b), Field-aligned currents in the dayside cusp observed by Triad, *J. Geophys. Res.*, *81*, 5971–5979, doi:10.1029/JA081i034p05971.

Iijima, T., and T. A. Potemra (1978), Large-scale characteristics of field-aligned currents associated with substorms, *J. Geophys. Res.*, *83*(A2), 599–615, doi:10.1029/JA083iA02p00599.

Ishii, M., M. Sugiura, T. Iyemori, and J. A. Slavin (1992), Correlation between magnetic and electric field perturbations in the field-aligned current regions deduced from DE 2 observations, *J. Geophys. Res.*, *97*(A9), 13,877–13,887, doi:10.1029/92JA00110.

Kamide, Y., and S.-I. Akasofu (1983), Notes on the auroral electrojet indices, *Rev. Geophys.*, *21*(7), 1647–1656, doi:10.1029/RG021i007p01647.

Kervalishvili, G. N., and H. Lühr (2013), The relationship of thermospheric density anomaly with electron temperature, small-scale FAC, and ion up-flow in the cusp region, as observed by CHAMP and DMSP satellites, *Ann. Geophys.*, *31*(3), 541–554, doi:10.5194/angeo-31-541-2013.

Kissinger, J., R. L. McPherron, T.-S. Hsu, and V. Angelopoulos (2011), Steady magnetospheric convection and stream interfaces: Relationship over a solar cycle, *J. Geophys. Res.*, *116*, A00I19, doi:10.1029/2010JA015763.

Kivelson, M. G., and D. J. Southwood (1991), Ionospheric traveling vortex generation by solar wind buffeting of the magnetosphere, *J. Geophys. Res.*, *96*(A2), 1661–1667, doi:10.1029/90JA01805.

Lühr, H., M. Rother, W. Köhler, P. Ritter, and L. Grunwaldt (2004), Thermospheric up-welling in the cusp region: Evidence from CHAMP observations, *Geophys. Res. Lett.*, *31*, l06805, doi:10.1029/2003GL019314.

Lühr, H., J. Park, J. W. Gjerloev, J. Rauberg, I. Michaelis, J. M. G. Merayo, and P. Brauer (2015), Field-aligned currents' scale analysis performed with the Swarm constellation, *Geophys. Res. Lett.*, *42*, 1–8, doi:10.1002/2014GL062453.

McWilliams, K. A., J. B. Pfeifer, and R. L. McPherron (2008), Steady magnetospheric convection selection criteria: Implications of global SuperDARN convection measurements, *Geophys. Res. Lett.*, *35*, L09102, doi:10.1029/2008GL033671.

Milan, S. E., G. Provan, and B. Hubert (2007), Magnetic flux transport in the Dungey cycle: A survey of dayside and nightside reconnection rates, *J. Geophys. Res.*, *112*, A01209, doi:10.1029/2006JA011642.

Miura, A., and T. Sato (1980), Numerical simulation of global formation of auroral arcs, *J. Geophys. Res.*, *85*(A1), 73–91, doi:10.1029/JA085iA01p00073.

Murphy, K. R., I. R. Mann, I. J. Rae, C. L. Waters, B. J. Anderson, D. K. Milling, H. J. Singer, and H. Korth (2012), Reduction in field-aligned currents preceding and local to auroral substorm onset, *Geophys. Res. Lett.*, *39*, L15106, doi:10.1029/2012GL052798.

Nagatsuma, T., H. Fukunishi, H. Hayakawa, T. Mukai, and A. Matsuoka (1996), Field-aligned currents associated with Alfven waves in the poleward boundary region of the nightside auroral oval, *J. Geophys. Res.*, *101*(A10), 21,715–21,729, doi:10.1029/96JA01797.

Neubert, T., and F. Christiansen (2003), Small-scale, field-aligned currents at the top-side ionosphere, *Geophys. Res. Lett.*, *30*(19), 2010, doi:10.1029/2003GL017808.

Newell, P. T., C.-I. Meng, D. G. Sibeck, and R. Lepping (1989), Some low-altitude cusp dependencies on the interplanetary magnetic field, *J. Geophys. Res.*, *94*(A7), 8921–8927, doi:10.1029/JA094iA07p08921.

Olsen, N., et al. (2013), The Swarm Satellite Constellation Application and Research Facility (SCARF) and Swarm data products, *Earth Planets Space*, *65*(11), 1189–1200, doi:10.5047/eps.2013.07.001.

Ritter, P., and H. Lühr (2006), Curl-B technique applied to Swarm constellation for determining field-aligned currents, *Earth Planets Space*, *58*, 463–476.

Rother, M., K. Schlegel, and H. Lühr (2007), CHAMP observation of intense kilometer-scale field-aligned currents, evidence for an ionospheric Alfvén resonator, *Ann. Geophys.*, *25*, 1603–1615, doi:10.5194/angeo-25-1603-2007.

Sato, N., D. M. Wright, C. W. Carlson, Y. Ebihara, M. Sato, T. Saemundsson, S. E. Milan, and M. Lester (2004), Generation region of pulsating aurora obtained simultaneously by the FAST satellite and a Syowa-Iceland conjugate pair of observatories, *J. Geophys. Res.*, *109*, A10201, doi:10.1029/2004JA010419.

Sibeck, D. G. (1990), A model for the transient magnetospheric response to sudden solar wind dynamic pressure variations, *J. Geophys. Res.*, *95*(A4), 3755–3771, doi:10.1029/JA095iA04p03755.

Waters, C. L., B. J. Anderson, and K. Liou (2001), Estimation of global field aligned currents using the Iridium® system magnetometer data, *Geophys. Res. Lett.*, *28*(11), 2165–2168, doi:10.1029/2000GL012725.